Improving Cell Seeding Efficiency through Modification of Fiber Geometry in 3D Printed Scaffolds

V.L. Mainardi[1,2], C. Arrigoni[1*], E. Bianchi[2*], G. Talò[3], M. Delcogliano[4], C. Candrian[4], G. Dubini[2], M. Levi[5], M. Moretti[1,3,#]

[1]Regenerative Medicine Technologies Lab, Ente Ospedaliero Cantonale (EOC), Via Tesserete 46, 6900 Lugano, Switzerland

[2]Laboratory of Biological Structures Mechanics (LaBS), Department of Chemistry, Materials and Chemical Engineering "Giulio Natta", Politecnico di Milano, Piazza Leonardo da Vinci 32, 20133 Milan, Italy

[3]Cell and Tissue Engineering Laboratory, IRCCS Istituto Ortopedico Galeazzi, via Galeazzi, 4, 20161 Milan, Italy

[4]Unità di Traumatologia e Ortopedia, Ente Ospedaliero Cantonale (EOC), Via Tesserete 46, 6900 Lugano, Switzerland

[5]Department of Chemistry, Materials and Chemical Engineering "Giulio Natta", Politecnico di Milano, Piazza Leonardo da Vinci 32, 20133 Milan, Italy

[*]Equally contributing authors

[#]Corresponding author: matteo.moretti@eoc.ch

Regenerative Medicine Technologies Lab, Ente Ospedaliero Cantonale (EOC), Via Tesserete 46, 6900 Lugano, Switzerland

Abstract

Cell seeding on 3D scaffolds is a very delicate step in tissue engineering applications, influencing the outcome of the subsequent culture phase, and determining the results of the entire experiment. Thus, it is crucial to maximize its efficiency. To this purpose, a detailed study of the influence of the geometry of the scaffold fibers on dynamic seeding efficiency is presented. 3D printing technology was used to realize PLA porous scaffolds, formed by fibers with a non-circular cross-sectional geometry, named multilobed to highlight the presence of niches and ridges. An oscillating perfusion bioreactor was used to perform bidirectional dynamic seeding of MG63 cells. The fiber shape influences the fluid dynamic parameters of the flow, affecting values of fluid velocity and wall shear stress. The path followed by cells through the scaffold fibers is also affected and results in a larger number of adhered cells in multilobed scaffolds compared to scaffolds with standard pseudo cylindrical fibers. Geometrical and fluid dynamic features can also have an influence on the morphology of adhered cells. The obtained results suggest that the reciprocal influence of geometrical and fluid dynamic features and their combined effect on cell trajectories should be considered to improve the dynamic seeding efficiency when designing scaffold architecture.

Keywords: Cell seeding, 3D printing, Bioreactor, Porous scaffold, Fiber geometry

1. Introduction

Tissue Engineering (TE) is a multidisciplinary field, which aims at developing biological substitutes for the treatment of damaged tissues, combining three main components: cells, that represent the essential element for the production of biological constructs, scaffolds, that provide a 3D support during construct maturation, and bioreactors, that can be used as conditioning systems for the

dynamic stimulation of the developing construct and as tools for automating construct development [1–3].

Cell seeding on 3D scaffolds is a crucial step in TE applications and influences the outcome of all the subsequent phases [4]. Traditionally, it is performed manually, loading the cells in the upper part of the scaffold and relying on gravity force to let cells move towards the inner core of the structure [5]. Despite the simplicity, this method leads to inhomogeneous distribution of cells that cannot penetrate properly, especially when thick and low-porosity scaffolds are used. Therefore, perfusion bioreactors are designed not only to stimulate the growing tissue, but also to dynamically seed cells on scaffolds, aiming at enhancing the homogeneity of cell distribution [6,7]. This approach leads to an improvement of cell penetration, while favoring the reproducibility and the automatization of the seeding phase to reduce intra- and inter-user variability [8,9]. However, the use of perfusion bioreactors often results in lower seeding efficiency when compared to static seeding.

3D printing is an Additive Manufacturing (AM) technique, increasingly used in biomedical applications. It comprises several techniques, such as Fused Deposition Modeling (FDM) and stereolithography (SLA) sharing the same working principle. Briefly, physical three-dimensional objects are fabricated through a layer-by-layer approach, generally starting from a digital model [10]. FDM is an extrusion-based technique, which uses a heated nozzle to deposit fibers of thermo-sensible materials [11,12]. SLA is a photopolymerization-based technique, which uses a spatially controlled irradiation to solidify liquid resins [13,14]. Thanks to the possibility to precisely control the structure of printed objects, these techniques are being used for several biomedical purposes, ranging from the fabrication of organ models for preoperative planning of surgery to the production of biocompatible scaffolds for TE applications [15–17]. FDM is a low-cost technology that does not require complex instruments and setups and offers the possibility to easily print 3D objects directly from a CAD model,

in single piece and customized models, choosing among a wide range of biocompatible materials. For these reasons, it has been applied to produce fibrous scaffolds characterized by customized architecture and porosity. The shape of the nozzle in FDM-based 3D printers allows the deposition of cylindrical fibers that are arranged to form structures with open pores. However, the main drawback of these scaffolds, characterized by standard cylindrical fibers, is that they often generate an inadequate number of adherent cells when the seeding phase is performed dynamically using a bioreactor. Several works have been published assessing the effects of overall scaffold geometry on cell seeding[18–22]. A typical approach that has been used consists in the variation of the disposition of cylindrical fibers within the 3D structure [23] However, the resulting modification of the internal geometry of the scaffold fails to ensure a sufficient and homogeneous seeding.

The aim of this study is to demonstrate that changing the cross-sectional shape of the single fiber in 3D printed scaffolds affects the outcome of cell seeding in porous scaffolds. This new approach can help improve the efficiency and homogeneity of dynamic cell seeding processes.

2. Materials and methods

To study the role of fiber cross-sectional shape in scaffolds made of assembled fibers, a multi-approach investigation was performed by combining experimental and computational tools. Experimental investigations were performed to 1) evaluate the pathways of cells flowing through the scaffolds, designing dedicated microfluidic chips, and 2) assess the dynamic seeding efficiency, by seeding cells with a perfusion bioreactor. Computational Fluid Dynamics (CFD) simulations were performed to describe the fluid dynamic environment inside the scaffolds and predict the effect of fiber cross-sectional shape on flow characteristics. Micro Particle Imaging Velocimetry (μPIV) experiments were performed to show the actual behavior of flow around the fiber geometry replicas, in microfluidics chips.

2.1. Design and 3D printing of multilobed scaffolds

To design cylindrical, multilobed scaffolds, a computer aided design software (SolidWorks, Dassault Systèmes, Vélizy-Villacoublay, France) was used. Multiple cylindrical fibers were assembled to form composite fibers, hereinafter named multilobed fibers, characterized by a non-circular cross-sectional geometry (Figure 1(a)). Four different multilobed scaffolds were designed with a diameter of 8 mm and a height of 4 mm. Fibers were assembled in ordered layers, overlaid to create the scaffolds, and were named 'circular', used as control, 'bilobed', 'trilobed' and 'quadrilobed', (Figure 1(b)). The distance between parallel multilobed fibers of the same layer was set to 400 μm to maintain constant pore dimension. The distance between subsequent layers was dependent on the multilobed fiber thickness, while the angle between fibers of adjacent layers was set to 90°.

A custom script was developed in Matlab (The MathWorks Inc., Natick, MA, USA) to convert the scaffold model into G-Codes, necessary for the printing process.

A fused deposition modeling-based 3D printer (BFB 3000, 3D Systems, Rock Hill, SC, USA) equipped with a 500 μm nozzle and loaded with a polylactic acid (PLA) filament (RS PRO, Milan, Italy) was used to print the scaffolds through a layer-by-layer approach. According to values found in the literature, the printing temperature was set to 195 °C and the printing speed was set to 300 mm/min [24–26].

Multilobed fibers were realized depositing parallel standard cylindrical fibers on the first layer and completing the multilobed structures depositing other standard cylindrical fibers on subsequent layers (Figure 2(a,b)). After printing, the scaffolds were sterilized with 70% ethanol for 30 min, twice rinsed with distilled water for 10 min, dried and properly stored until use.

An analogous approach was used to design and print circular and trilobed scaffolds using a custom

made 250 μm nozzle (SITEC - Politecnico di Milano) for the deposition of multilobed fibers in a single extrusion process (Figure 6(a,b)).

2.2. Design and fabrication of microfluidic chips

A computer aided design software (SolidWorks, Dassault Systèmes, Vélizy-Villacoublay, France) was used to design the molds for the fabrication of microfluidic devices, representing a volumetric section of the whole structure of the analyzed scaffolds. In particular, a structure characterized by a 7×7 array of 100 μm high pillars was designed for each configuration of the scaffolds, within a rectangular channel with 3 mm height and side width dependent on specific chip configuration (Figure 1(e,h)).

To fabricate the molds through a layer-by-layer approach, a digital light processing-based 3D printer (MAX, Asiga, Sidney, Australia) equipped with a resin tank filled with a photopolymer (DentaModel, Asiga, Sydney, Australia) was used, dividing the models in layers 50 μm high through a slicing software (Composer, Asiga, Sidney, Australia). The printing parameters were set accordingly to the material datasheet, except for exposure time and burn-in exposure time, which were set equal to 0.338 and 3 s respectively, and burn-in layer, which was set equal to 2. After printing, the molds were detached from the printing platform and transferred successively in two glass beakers filled with 70% isopropanol and one glass beaker filled with distilled water to wash the uncured resin. Then, compressed air was used to dry the molds and remove any unwanted residual. To complete the post-curing of the resin, the molds were transferred in a transparent Petri dish filled with distilled water and moved into the tray of an UV curing chamber (FLASH, Asiga, Sydney, Australia) for 20 min. Then, after drying with compressed air, a second 20 min cycle of UV curing was performed transferring the molds directly into the tray of the curing chamber. Subsequently, accordingly to

standard practice, the molds were placed in a vacuum chamber and exposed to silane vapors for 30 min [27,28]. Finally, microfluidic chips were obtained by casting a mixture 10% w/w of polydimethylsiloxane (PDMS) and crosslinking agent (SYLGARD^{TM} 184, Dow Corning, Midland, MI, USA) on the corresponding molds and heating it at 80 °C for 2 h. Once complete polymerization occurred, microfluidic chips were detached from the molds, cleaned through three successive washings in acetone, isopropanol, and distilled water, dried with compressed air, bonded to glass coverslips through plasma activation and properly stored until use.

2.3. Computational simulations

To estimate the local fluid velocity within the scaffolds and the distribution of wall shear stresses on fiber surfaces, fluid dynamic computational steady-state simulations were performed using a finite volume method (FVM) software (ANSYS Workbench, ANSYS Inc., Canonsburg, PA, USA). To reduce the global computational cost for each investigated fiber design, a representative volume was selected in order to perform simulations with periodic conditions at the boundaries (Figure 1(d), **Errore. L'origine riferimento non è stata trovata.**). These settings are suitable when the expected pattern of the flow solution has a periodically repeating nature, consistently with the geometrical structures of this kind of fiber scaffolds. Symmetries on geometrical planes parallel to main direction of flow were exploited to set symmetry boundary conditions. Geometrical symmetry planes at inlet and outlet cross sections were used to set periodic translational conditions of velocity and pressure. On the fiber surfaces a no-slip condition was set, where velocity of fluid was constrained to zero. Tetrahedral grids were generated using ANSYS Meshing (ANSYS Inc., Canonsburg, PA, USA), dividing the simulated volumes into up to 1.8 M elements.

The culture medium was modeled as an aqueous fluid with density and viscosity at 37 °C equal to

1000 kg/m^3 and 8.1×10^{-4} Pa·s, respectively [29]. Inlet mass flow rate was defined in order to match the experimental condition of 1000 μm/s, as set in the bioreactor. Additional information regarding the simulation pipeline are reported in Supplementary section.

The fluid dynamic quantities of interest were velocity, wall shear stresses and deceleration volumes. Deceleration volumes were considered as locations in which the fluid velocity decreases below a reference threshold, set equal to the 5% of bioreactor working velocity.

2.4. Geometrical characterization

A geometrical characterization was performed assessing values of scaffold porosity and permeability. Porosity was calculated as the ratio between the volume of the solid scaffold and the volume of a cylinder with the same height. Volume of solid scaffold is the total volume of fibers and was calculated based on the weight of the scaffold, the measured height and the known PLA density [30].

Permeability was measured through an in-house permeameter, previously described, based on Darcy's law and used with distilled water at room temperature [31].

2.5. Experimental setups

2.5.1. Perfusion bioreactor

To perform dynamic seeding and culturing experiments, an oscillating perfusion bioreactor (OPB) was used, as previously described [31–35]. Briefly, it consists in an oscillating platform on which culture chambers are placed, formed by medical-grade silicone tubes (TYGON®, Saint-Gobain, Curbevoie, France). Within the chamber a PDMS support holds the scaffold, which is constantly perfused by the cell solution that flows through its fibers under the effect of the bidirectional oscillation of the chamber about its central axis (Figure 1(f,g)).

2.5.2. *Cell seeding and culturing*

MG63 bone-derived cells were commercially obtained and cultured for 5 days in Dulbecco's modified Eagle medium (DMEM; 1 g/l glucose, Life Technologies), 10% FBS, 4 mM L-glutamine, 1 mM sodium pyruvate, 1 U/ml penicillin and 1 µg/ml streptomycin (all from Sigma-Aldrich, St. Louis, MO, USA). Before the seeding, cells were trypsinized for 4 minutes, counted and resuspended in the same medium to get a concentration of 1 Mcells/ml. Then, 2 ml of cell solution were transferred in the bioreactor chambers, which were filled with 8 ml of medium to reach a total amount of 10 ml per chamber, and 2 ml of cell solution were transferred in a 15 ml Falcon tube and stored as a reference value for the calculation of the seeding efficiency [31]. Subsequently, the complete chambers were incubated for 24 hours to perform the seeding experiments setting a perfusion velocity of 1000 µm/s and an oscillation amplitude of 270° through the bioreactor control system, corresponding to a flow rate of 1.9 ml/min. To perform the culturing experiments, the same setup described for the seeding experiment was used for the first 24 hours. The day after, the perfusion velocity was decreased to 100 µm/s and the chambers were maintained in incubation until day 7. The medium was completely changed after the seeding, namely day 1, and after 3 days of culture. At the end of the experiments, seeding efficiency was calculated as the amount of DNA found on the seeded scaffolds divided by the amount of DNA of the reference control aliquot.

Primary cells were also tested with our multilobed approach. Specifically, human chondrocytes derived from waste material from knee prosthesis patients under an Ethic Committee permission and commercial human skin fibroblasts (Angioproteomie, Boston, MA, USA).

2.5.3. *Alamar Blue assay*

Cell viability of MG63 was determined at day 1, 4 and 7, using alamarBlue™ Cell Viability Reagent (Life Technologies, Carlsbad, CA, USA). For each condition, at least three samples were moved from

the bioreactor chambers and transferred in a 24 well plate. After a rinsing in phosphate buffer saline (PBS) (Life Technologies, Carlsbad, CA, USA), each sample was incubated for 3.5 hours in 1 ml of a solution obtained mixing 10% v/v of alamarBlue™ reagent in Red Phenol Free DMEM (Life Technologies, Carlsbad, CA, USA). Subsequently, 200 µl of alamarBlue™ were transferred in triplicate in a black 96 well plate and fluorescence emission at 540 nm was assessed using a spectrophotometer (VICTOR X3, PerkinElmer, Waltham, MA, USA). After the cell viability assay, the samples were rinsed in PBS and stored for further analyses.

2.5.4. CyQuant assay

Prior to quantifying DNA content, a digestion with proteinase K was performed [36]. Briefly, 100 mg of proteinase K (Sigma-Aldrich, St. Louis, MO, USA), 605.7 mg of TRIZMA base (Sigma-Aldrich, St. Louis, MO, USA), 1 ml of EDTA + Iodoacetamide solution and 500 µl of Pepstatin A solution were mixed in ddH_2O reaching 100 ml in volume. Adding HCl 1M, the solution pH was brought to 7.6. Then, 500 µl of proteinase K solution were used to digest each sample for 16 hours at 56 °C using a thermomixer.

DNA content was determined at day 0, 3 and 7 using CyQuant kit (Life Technologies, Carlsbad, CA, USA). For each sample 195 µl of proteinase K solution and 5 µl of CyQuant solution were transferred in triplicate in a black 96 well plate and CyQuant fluorescence at 520 nm was assessed using a spectrophotometer (VICTOR X3, PerkinElmer, Waltham, MA, USA).

2.5.5. Immunostaining

Immunostaining was performed to evaluate the distribution of adhered cells on the scaffold surface. Samples were fixed in 4% paraformaldehyde for 15 min at room temperature and rinsed with PBS. Subsequently, samples were permeabilized with 2% BSA (Sigma-Aldrich, St. Louis, MO, USA) and 0.2% Triton-X 100 (Sigma-Aldrich, St. Louis, MO, USA) for 30 min at room temperature. Next, a

solution containing Alexa Fluor™ 488 Phalloidin (Thermo Fisher, Waltham, MA, USA) and 4'6-Diamidino-2-Phenylindole (DAPI) in PBS was added to the samples and incubated at 37 °C for 1 h. Finally, samples were twice rinsed in PBS and observed under a fluorescence microscope.

2.6. µPIV experiments

Fluid dynamic fields of fluid velocity around the fiber-shaped pillars, inside microfluidic PDMS chips, were observed by µPIV imaging. The 2D µPIV system (TSI Incorporated, Minneapolis, USA), composed by an inverted microscope (Olympus IX71), a laser (Nd:YAG 532 nm), and a camera (Power View 4M, 2048 9 2048 pixels), allowed calculation of the velocity field based on the correlation of fluorescent images, acquired with a known and proper time lapse (Δt). Excited by the laser, light emitted by fluorescent tracer particles ($Ø_p$ = 1 µm, Thermo Fisher Scientific, Waltham, MA, USA, 1% solids, re-suspended 1:10 in distillated water solution) was recorded by the synchronized camera and elaborated by means of a dedicated algorithm.

The experimental setup was composed by a syringe pump (PHD2000, Harvard Apparatus, Holliston, MA, USA), a 5 ml glass syringe (Gastight Syringes, Hamilton Bonaduz AG, Switzerland) with a 18 G needle connected with PTFE tubing, that was then directly inserted into the PDMS test chamber. 70 couples of images (10x magnification) for each field of observation were elaborated to build each flow field (calibration of 0.46 µm/px, interrogation areas 32 x 32 pixel). Acquisition time was tuned from 250 to 2300 µs, in order to catch the range of velocity up to 7.5 mm/s.

2.7. Cell tracking

To perform the experiments for cell tracking, firstly microfluidic chips were filled in vacuum with PBS. Then, the microfluidic chip inlet was connected to a programmable syringe pump (PHD2000, Harvard Apparatus, Holliston, MA, USA) through a 5 ml syringe (BD, Franklin Lakes, NJ, USA) and

a silicon tube (Ø = 0.76 mm, L = 1.3 m), filled with 2.5 ml of PBS, while the outlet was connected to a 1.5 ml Eppendorf tube through a silicon tube (Ø = 0.76 mm, L = 1.3 m). When the whole system was filled with PBS, the inlet tube was detached from the chip, refilled with 500 µl of a MG63 cells, suspended in the same medium used for cell seeding experiments at a concentration of 1 Mcells/ml. Then, the syringe pump was used to run the experiments with a flow rate dependent on chip configuration, which resulted in fluid velocities comparable with those found in the OPB bioreactor (1000 µm/s). Generated by the syringe pump, a flow of cells suspension entered the microfluidic chip through the inlet tube. Cells flowed through the array of pillars along one direction, and then left the microfluidic chip washed out through the outlet tube. The path followed by cells was registered under a microscope in bright field through a high-speed camera (MIRO 2M, Phantom, Wayne, NJ, USA) with a resolution of 640x480 px at 900 fps.

For cell tracking the plugin TrackMate v3.8.0 of Imagej (NIH, Bethesda, MD, USA) was applied to the recorded movies using LoG detector to localize cells in each frame and Simple LAP tracker to extract cell trajectories [37]. Subsequently, a custom script was developed in Matlab (The MathWorks Inc., Natick, MA, USA) to analyze trajectory characteristics comparing the different microfluidic chip configurations.

A set of 900 frames for a total time of 5 s was analyzed for each geometrical experimental configuration. In particular, a central pillar was selected for the analysis of cell paths to avoid boundary effects. A fluid dynamic evaluation was performed to assess values of deceleration area on the middle plane perpendicular to the pillar direction using the same reference threshold previously reported. A deceleration area around the pillar, defined by means of deceleration velocity threshold (0.05 mm/s), was extrapolated from dedicated CFD simulations and superimposed to the cell

trajectories to extract the number of cells that reach the deceleration area every second, defined as decelerating cells.

2.8. Statistical analysis

Analysis of variance (ANOVA) was performed with Prism (GraphPad Software Inc., San Diego, CA, USA). ANOVA was followed by Bonferroni post-hoc test to determine significant differences between groups. Differences were considered significant for $p < 0.05$ (*), $p < 0.01$ (**) and $p < 0.005$ (***). Results are presented as mean ± standard deviation considering at least 3 samples per experimental condition.

3. Results

3.1. Geometrical characterization

Stereo microscopic images of fiber sections and scaffolds showed that through the selected printing parameters it was possible to produce 3D cylindrical structures with features comparable to those of designed models (Figure 2(a,b)). To quantify the differences in geometrical parameters, diameters and perimeters of scaffold fiber sections were measured. Obtained results showed that PLA fibers swelled after the deposition due to the extrusion pressure, resulting slightly wider than the nozzle dimensions. Fiber diameters ranged from 545±27 μm for quadrilobed fibers to 587±29 μm for circular fibers, with bilobed and trilobed fibers showing values equal to 582±41 μm and 578±24 μm, respectively (Figure 2(c)).

Then, the perimeter of scaffold fibers was assessed. Total fiber perimeters increased, as expected, from 1931±109 μm for single circular fibers to 4936±83 μm for quadrilobed fibers (Figure 2(d)).

Then, each configuration for designed and printed scaffolds was characterized assessing values of porosity and permeability. Porosity values ranged from a minimum value of 48.27±3.37% for bilobed

scaffolds to a maximum of 63.44±0.27% for quadrilobed scaffolds, while circular and trilobed scaffolds showed intermediate values of porosity equal to 58.59±0.37% and 59.89±0.20%, respectively (Figure 2(e)).

The same trend was found assessing permeability values. Bilobed scaffolds showed the minimum permeability value (327.97±4.56 Darcy), while the maximum value was found in quadrilobed scaffolds (658.36±3.66 Darcy). Circular and trilobed scaffolds showed values of permeability in between 585.44±5.76 Darcy and 572.94±2.91 Darcy, respectively (Figure 2(f)).

Scaffolds were also printed using a custom-made nozzle that allowed the production of trilobed fibers within a single extrusion, thus avoiding the assembling approach, achieving a reduced fiber scale and making the dimensions of different geometries comparable. Stereo microscopic images of fiber sections showed that also through the custom-made nozzle it was possible to extrude cylindrical and non-cylindrical fibers, resembling the designed models (Figure 6(a,b)). Measured values of diameter were equal to 257.99±5.29 μm and 291.85±17.16 μm for circular and trilobed fibers, respectively, while measured values of perimeter were equal to 810.49±16.61 and 806.22±39.28 μm for circular and trilobed fibers, respectively (Figure 6(c)).

3.2. Biological results

3.2.1. Seeding and culturing results

CyQuant assay was performed to evaluate the outcome of seeding experiments after 1 day, while for the culturing experiments CyQuant assay was performed 1, 3 and 7 days after the seeding, namely T1, T4 and T7, respectively. The results showed that there was a significant difference ($p<0.005$) between trilobed and circular scaffolds in terms of seeding efficiency with values of trilobed scaffolds 3.61-fold higher than values for circular scaffolds. Bilobed and quadrilobed scaffolds showed,

respectively, a seeding efficiency 1.25-fold and 1.32-fold higher than the seeding efficiency of circular scaffolds, but in both cases the difference with other fiber shapes was not statistically significant (Figure 3(a)).

The same trend was found analyzing the seeding efficiency of circular and trilobed scaffolds printed using the 250 μm nozzle. Obtained results show that the seeding efficiency of trilobed scaffolds was 1.65-fold higher than the seeding efficiency of circular scaffolds (Figure 6(d)). However, in this case the difference was not statistically significant.

A trend similar to that observed for MG63 was found for human chondrocytes and human skin fibroblasts, although the difference was not statistically significant. In particular, the values of seeding efficiency were 2.07-fold and 2.67-fold higher for the trilobed scaffolds as compared to the circular control scaffolds for chondrocytes and fibroblasts, respectively (**Errore. L'origine riferimento non è stata trovata.**(a)).

Regarding the culturing experiments, cellular growth rate found in circular and trilobed scaffolds after 4 and 7 days of dynamic culture was comparable when evaluating the relative number of cells present on the scaffolds at day 1. This result suggests that the use of multilobed fibers has not a detrimental effect on the growth of adhered cells (**Errore. L'origine riferimento non è stata trovata.**).

3.2.2. Cell viability

Alamar Blue assay was performed to evaluate cellular viability 24 h after dynamic seeding. As expected, the trend followed that of seeding efficiency values. The obtained results showed that there was a significant difference ($p<0.01$) between trilobed and circular scaffolds in terms of cell viability with values of trilobed scaffolds 2.15-fold higher than values for circular scaffolds. Bilobed and quadrilobed scaffolds showed, respectively, a cell viability 1.19-fold and 1.27-fold higher than the cell viability of circular scaffolds, but in both cases the difference was not statistically significant

(Figure 3(b)). Consistently, the same trend was found in the scaffolds printed with the 250 μm nozzle. Trilobed scaffolds showed a cell viability 1.62-fold higher than circular scaffolds (Figure 6(d)). However, the difference was not statistically significant according to the selected statistical method. For human chondrocytes, a similar trend was found with values of viability of cells seeded on trilobed scaffolds 1.59-fold higher than those seeded on circular control scaffolds. However, for human skin fibroblasts, the values of viability of cells seeded on trilobed and circular scaffolds were comparable (1.01-fold higher in trilobed scaffolds) (**Errore. L'origine riferimento non è stata trovata.**(b)).

3.2.3. Immunostaining

To assess cell distribution on scaffold fibers an immunostaining was performed, combining DAPI and phalloidin. Fluorescence images revealed the presence of cells along all the fiber in bilobed and trilobed scaffolds within the analyzed portion, while cells were confined in isolated areas in circular and quadrilobed scaffolds (Figure 3(c,d)). In particular, the highest density of cells in multilobed scaffolds was observed inside the niches formed between two parallel cylindrical fibers, while cell presence was not observed in fiber lateral ridges.

Interestingly, our multilobed approach influenced not only the distribution but also the morphology of adhered cells. Fluorescence images taken at higher magnification (20x) revealed that cells tended to align to the fibers spreading their cytoskeleton parallel to the fiber axis direction in multilobed scaffolds, while showing a more rounded shape in circular fiber scaffolds (Figure 3(e)). However, although this phenomenon was easily observable for bilobed and trilobed configurations, it was less evident in quadrilobed configuration.

3.3. Fluid dynamic evaluation

A fluid dynamic evaluation of the scaffolds was performed through CFD simulations, assessing

values of fluid velocity within the porous structure, wall shear stress distribution on the scaffold fibers, and deceleration volume. Quadrilobed fibers showed the minimum mean value of fluid velocity (2.24 mm/s, median 2.39 mm/s, max 5.22 mm/s), while bilobed fibers showed the maximum mean value (5.86 mm/s, median 6.31 mm/s, max 11.63 mm/s). Intermediate values were found in circular and trilobed fibers (2.90 mm/s, median 3.21 mm/s, max 4.90 mm/s and 2.94 mm/s, median 3.05 mm/s, max 6.73 mm/s, respectively) (Figure 4(a,d)). As expected, maximum values were located in the middle of the pores among the fibers while the minimum values, down to zero, were located closed to the surfaces and between the fibers aligned in the main direction of flow.

Wall shear stress mean values ranged from 13.95 mPa for quadrilobed fibers (median 8.62 mPa, max 58.61 mPa) to 22.92 mPa for circular fibers (median 20.37 mPa, max 56.72 mPa), while bilobed and trilobed fibers showed mean values in between (22.64 mPa, median 7.59 mPa, max 132.24 mPa and 17.33 mPa, median 9.47 mPa, max 73.75 mPa, respectively) (Figure 4(b,e)). The regions with the highest values of shear stresses were located on the ridges exposed to the flow of bilobed fibers. In the same location all the fiber configurations showed the highest values of shear stress while the minimum values, down to zero, were located closed to the fiber to fiber connections and on the surfaces among the fibers aligned in the main direction of flow.

Deceleration volume was defined as the region of fluid characterized by a velocity below a certain threshold, set equal to 0.05 mm/s (i.e. 5% of bioreactor working velocity). Obtained results showed that bilobed scaffolds were characterized by the highest value of deceleration volume (6.23%), while the smallest value was found in circular scaffolds (0.49%). Following the trend of wall shear stresses, trilobed scaffolds showed an intermediate value of deceleration volume, equal to 4.11% (Figure 4(c,f)).

The 3D regions where velocity magnitude is lower than the defined threshold, were located in the

niches generated by the combination of circular units. These regions were particularly extended where side fibers lay on the same plane perpendicular to the main direction of flow, as in the bilobed and in the trilobed configurations. Such regions are absent in the circular configuration, where the calculated volume corresponds to the layer of fluid over the whole surface, with the velocity magnitude approaching the value of zero defined everywhere on the surface.

3.4. µPIV analyses

µPIV analyses allowed us to observe the flow field inside the microfluidic chips, especially all around the multilobed fiber-shaped obstacles. Due to the absence of three-dimensional structures, the regions with the highest velocity were smaller than the regions observed in the 3D simulations and were located between two adjacent fibers, in the same rank. Further elaborations of the µPIV data showed the distribution of transversal velocities (Figure 5(a)): bilobed and trilobed fibers were associated to higher transversal velocity values, estimated as the magnitude of vectors in the X direction (main flow is in direction of Y). Transversal velocity regions were located all around the lateral ridges. The maps of transversal velocity were symmetrical upstream and downstream the fibers with a symmetrical shape on the XZ plane. Differently from the circular, bilobed and quadrilobed fibers, trilobed fibers showed a different map of transversal velocity upstream and downstream the lateral ridge. Moreover, the asymmetry of the fiber shape on plane XZ led to a change of velocity distribution when the flow direction was reversed, as it happens in the bioreactor once every 40 s.

3.5. Analysis of cell trajectories

Superimposition of experimental (cell trajectories) and computation (deceleration areas) results showed that the number of decelerating cells per second was 5.50-fold, 7.50-fold and on average 15.13-fold higher in quadrilobed, bilobed and trilobed fibers compared to circular fibers (Figure

5(b,c)). Since the shape of the trilobed fibers was not symmetrical, we tested those fibers in both directions and obtained a number of decelerating cells per second 11.40-fold higher than that of circular fibers, when the flow headed from the single fiber to the double fiber, and 18.87-fold higher when the flow was in double fiber-to-single fiber direction.

Analyzing the cell path around the fibers it was possible to distinguish two types of trajectories, characterizing the different fiber configurations. In the presence of circular and quadrilobed fibers cells tended to flow straight without undergoing any relevant change of direction. On the contrary, in the presence of bilobed and trilobed fibers, when the lobe of the fiber is perpendicular to the flow, cells underwent lateral movements and local trajectory inversions.

4. Discussion

FDM-based 3D printing was chosen for the fabrication of PLA porous scaffolds as it gave the possibility to precisely control the deposition of the fibers. To evaluate accuracy and reproducibility of the printing method, diameter and perimeter of the printed fibers were measured and compared with the dimensions of the nominal fiber models that were created considering the nozzle features. The mean percentage error between the diameter of the nozzle and the diameter of the printed fibers was 15%. Although fiber diameters were wider than expected, the obtained results demonstrated the reproducibility of the printing method, which showed a standard deviation lower than 5%. These results are in accordance with a previous study, in which authors reported a comparable mean percentage error (18%) after the characterization of 3D printed PLA scaffolds [38].

FDM-based 3D printing showed to be a fabrication system that allows the assembly of multilobed fibers in multiple geometrical variants, with a good shape fidelity, as demonstrated by mean circularity values of single fibers going from 0.98 for circular configuration to 0.94 for quadrilobed

configuration, and the large number of parameters allows the fine control on the local microstructure (hundreds of microns) of the scaffolds.

The geometrical features described in this paper as determinant to cell seeding improvement are not in the size scale of cells, but are 10-fold bigger, a scale able to affect secondary flows in the scaffolds. A number of studies have already demonstrated the influence of scaffold geometry and architecture on cellular behavior. Efforts were mostly made to understand the effect of porosity, pore size, fiber spacing and fiber orientation on both mechanical properties of the scaffold and biological performance including cell seeding and cell proliferation [23,39–41]. Indeed, it is well known how pore size, pore geometry and mechanical properties all influence cell behavior inside tissue engineered scaffolds [42]. However, in FDM printed scaffolds it is not possible to separately control these three variables, since modification in pore size and shape are obtained through changes in the orientation of fiber deposition, which in turns influences mechanical properties [40,43]. Printing fibers with a different cross-sectional shape but equivalent diameter would allow to modulate pore size and geometry independently, and without significantly influencing scaffold mechanical properties, achieving a higher flexibility in scaffold fabrication. However, to the best of our knowledge, there are no works assessing cell seeding dependence on the cross-sectional shape of the scaffold fiber. Furthermore, there are no works evaluating the local fluid dynamics around obstacles (external flows) assessing the deposition of particles at this size scale.

Similar problems have been investigated regarding microfluidic chips presenting a lateral cavity designed to trap a particle flowing in a main channel [44,45]. However, these works deal with internal flows and feature sizes similar to cell sizes, thus their results are not directly comparable to the results described in this paper.

Since multilobed fibers were realized assembling standard fibers, their surface area was larger than

that of the cylindrical fibers used as control (data not shown). To exclude that the increase in seeding efficiency was only due to increased available area, a normalization of the number of seeded cells on the scaffold internal surfaces was performed, which indicated that in such a setup there was not a relation between the available surface and the cell seeding efficiency. Furthermore, as a proof of concept, we realized custom nozzles through which multilobed fibers were printed in a single deposition. This method allowed us to print smaller fibers (Ø = 250 μm) and keep the available area of cylindrical and multilobed fibers comparable. Endorsing the observations made with larger fibers (Ø = 500 μm), the obtained results showed that difference in terms of seeding efficiency was preserved at a smaller scale, proving that increasing seeding efficiency was due to the fiber shape modification.

To demonstrate the applicability of our approach also on primary cells, we tested human chondrocytes and human skin fibroblasts. A similar trend to that observed for MG63 cells was found analyzing the seeding efficiency of multilobed scaffolds compared to circular control scaffolds. Differently from seeding efficiency, the values of viability of fibroblasts seeded on trilobed and circular scaffolds were comparable. However, it was demonstrated that Alamar Blue assay values do not always correlate well with CyQuant DNA quantification, especially for mesenchymal cell types, as compared to tumor cells [46].

Although scaffold topography affects cell response, the experimental outcome is strongly dependent on the resolution of the technology used to realize the scaffolds and, consequently, on the scale of topographical features compared to cell dimensions [47]. In this context, due to the high dimensional ratio fiber/cell, previous works assessing the effect of scaffold architecture reported that cell morphology is more influenced by material properties than scaffold features or that scaffold features influence more viability and proliferation of adherent cells than their morphology [40,48]. However,

our results suggested that the cross-sectional shape of the fiber could have an influence also on cell morphology and orientation, by modifying the fluid dynamic field around the structures. Indeed, seeded cells tended to align with the niche longitudinal direction in scaffolds characterized by multilobed fibers, while they showed a more rounded morphology and random orientation in scaffolds characterized by standard cylindrical fibers. This apparent contradiction with previous results is related to the fact that in those studies the scaffold architecture was modified by varying the orientation of the fibers, whilst in our study changes in fiber cross-sectional shape led to modifications of scaffold pore geometry and provided the fibers with sites that are more suitable for cell docking. Based on these considerations, we hypothesized that the seeding outcome was mainly guided by the fluid dynamics of cell suspension flowing through the scaffold pores, strictly related to the fiber shape. However, even if the experimental results showed a significant increment of seeding efficiency in one of the multilobed configurations, fluid dynamic evaluation by itself could not explain this difference when considering single parameters among those generally analyzed [49]. As expected, wall shear stress distribution showed peaks in correspondence of fiber ridges, a reason for the absence of seeded cells in those regions. On the contrary, within the niches formed between two fibers, where fluid velocity was lower, wall shear stress showed values that are up to two orders of magnitude lower than those found on fiber ridges. However, comparing the values of different configurations, a correlation was not found between wall shear stress and seeding efficiency. Superimposing the fiber areas characterized by low values of shear stress to the fluorescence images of the scaffolds, it was observed that the majority of seeded cells remained in a defined area in which shear stress values were below 5 mPa both in circular and multilobed configurations (**Errore. L'origine riferimento non è stata trovata.**). Although these results are in accordance with previous studies assessing the effect of flow-induced shear stress on cell adhesion and detachment both in microfluidic and macro-systems, they

could not explain the differences in terms of number of adhered cells [50–53].

Even the definition of a deceleration region consisting of a 10 μm thick area around the fiber walls, whose thickness increases in correspondence of fiber niches, failed to predict the experimental seeding outcome. Therefore, combining experimental and computational tools, an analysis was carried out aiming at obtaining a comprehensive explanation of the experimental phenomenon.

Biological experiments performed in microfluidic chips representing a volumetric section of the multilobed structures allowed highlighting cell trajectories around ridge and niche regions. Experimental parameters were optimized for the observation of paths followed by cells induced by different fiber shapes. The need to observe independently fluid and particles behavior was due to the fact that in proximity of an obstacle and of cavities/niches the particles suspended in the fluid (i.e. cells in aqueous medium) tend to follow trajectories that could be different from those followed by the fluid. This behavior is usually described by computing the Stokes number [21,54], but in our case it was not sufficient to define the difference among the analyzed fiber shapes because the characteristic dimension of the structures was comparable [8]. However, these experiments were useful to calculate the number of cells reaching the regions characterized by low velocity values around the multilobed structures and to analyze the differences among the paths followed by cells in the presence of different fiber configurations. Combining the information of fluid velocity and of cell number flowing through deceleration regions (CFD results), it was possible to observe a difference comparing the trilobed fiber with the other analyzed fibers. Trilobed fiber was the sole configuration being asymmetrical in the direction of flow. The transversal velocities around the obstacles showed different maps depending on the direction of the main flow. Since the bidirectional nature of the seeding process has been demonstrated to enhance cell seeding efficiency and uniformity, we hypothesized that the alternating fluid dynamic condition contributes to explain the seeding efficiency

value of this specific fiber shape [55].

5. Conclusions

In this study multilobed fibers characterized by a non-circular cross-sectional geometry, were extruded through an FDM-based 3D printer to realize cylindrical scaffolds for the evaluation of dynamic cell seeding. The fiber cross-sectional geometry strongly influences the fluid dynamic environment within the scaffolds affecting the values of flow velocity and distribution of shear stresses on scaffold fibers. As a consequence, by varying the fiber shape it was possible to modify the path followed by cells, enhancing the number of seeded cells in multilobed fiber scaffolds compared to standard circular fiber scaffolds. Tuning geometrical and fluid dynamic features also had an influence on the morphology of adhered cells, which tended to align with the niche longitudinal direction in multilobed scaffolds in our experiments.

These findings suggest that, during the design of scaffold architecture, the reciprocal influence of geometrical and fluid dynamic features and their combined effect on cell trajectories should be considered to improve the dynamic seeding efficiency. Combining different circular and multilobed fibers within the same scaffold can be a useful approach to control cell seeding distribution for applications in which a gradient in cell positioning is desired.

Since the same phenomenon was observed by reducing the dimensions of the fibers, our approach can be useful also for printing scaffolds characterized by smaller features. The proposed multilobed approach can be applied also to develop devices aimed at different applications, such as microfluidic chips for cell aggregate formation, cell sorting and cell trapping.

Our results represent a valuable knowledge toward the improvement of dynamic seeding efficiency that may be particularly helpful in all those applications whose aim is to maximize the number of

captured particles.

Acknowledgments

The authors would like to thank Dr. Ali Gökhan Demir (SITEC – Politecnico di Milano) for the prototyping of the nozzles, Dr. Gabriele Natale for the realization of the 250 μm scaffolds; PoliFab (Politecnico di Milano) for the support in an initial microfabrication step.

Funding

This research did not receive any specific grant from funding agencies in the public, commercial, or not-for-profit sectors.

References

[1] Langer R and Vacanti J P 1993 Tissue engineering *Science (80-.).* **260** 920–6

[2] Fisher J P, Mikos A G and Bronzino J D 2007 *Tissue Engineering* (Roca Raton: CRC)

[3] Akter F 2016 Principles of Tissue Engineering *Tissue Engineering Made Easy* (Cambridge: Academic Press) pp 3–16

[4] Mauck R L, Wang C C, Oswald E S, Ateshian G A and Hung C T 2003 The role of cell seeding density and nutrient supply for articular cartilage tissue engineering with deformational loading *Osteoarthr. Cartil.* **11** 879–90

[5] Villalona G A, Udelsman B, Duncan D R, McGillicuddy E, Sawh-Martinez R F, Hibino N, Painter C, Mirensky T, Erickson B, Shinoka T and Breuer C K 2010 Cell-seeding Techniques in Vascular Tissue Engineering *Tissue Eng Part B Rev* **16** 341–50

[6] Chen Y, Bloemen V, Impens S, Moesen M, Luyten F P and Schrooten J 2011 Characterization and optimization of cell seeding in scaffolds by factorial design: quality by design approach for skeletal tissue engineering *Tissue Eng Part C Methods* **17** 1211–21

[7] Beşkardeş I G, Aydın G, Bektaş Ş, Cengiz A and Gümüşderelioğlu M 2018 A systematic study for optimal cell seeding and culture conditions in a perfusion mode bone-tissue bioreactor *Biochem. Eng. J.* **132** 100–11

[8] Campos Marín A, Brunelli M and Lacroix D 2018 Flow perfusion rate modulates cell deposition onto scaffold substrate during cell seeding *Biomech Model Mechanobiol* **17** 675–87

[9] Schmid S, Schwarz S, Meier-Staude R, Sudhop S, Clausen-Schaumann H, Schieker M and Huber R 2018 A Perfusion Bioreactor System for Cell Seeding and Oxygen-Controlled Cultivation of Three-Dimensional Cell Cultures *Tissue Eng Part C Methods* **24** 585–95

[10] Lele A 2019 Additive Manufacturing (AM) *Disruptive technologies for the militaries and security* (Singapore: Springer) pp 101–9

[11] Liu Z, Wang Y, Wu B, Cui C, Guo Y and Yan C 2019 A critical review of fused deposition modeling 3D printing technology in manufacturing polylactic acid parts *Int J Adv Manuf Technol* **102** 2877–2889

[12] Rahim T N A T, Abdullah A M and Md Akil H 2019 Recent Developments in Fused Deposition Modeling-Based 3D Printing of Polymers and Their Composites *Polym. Rev.* **59** 589–624

[13] Salonitis K 2014 Stereolithography *Comprehensive Materials Processing* (Amsterdam: Elsevier) pp 19–67

[14] Skoog S A, Goering P L and Narayan R J 2014 Stereolithography in tissue engineering *J Mater Sci Mater Med* **25** 845–56

[15] Birbara N S, Otton J M and Pather N 2019 Modelling and Printing Technology to Produce Patient-Specific 3D Models *Hear. Lung Circ* **28** 302–13

[16] Bose S, Vahabzadeh S and Bandyopadhyay A 2013 Bone tissue engineering using 3D printing *Mater. Today* **16** 496–504

[17] Zhang L, Yang G, Johnson B N and Jia X 2019 Three-dimensional (3D) printed scaffold and material selection for bone repair *Acta Biomater* **84** 16–33

[18] Melchels F P, Barradas A M, van Blitterswijk C A, de Boer J, Feijen J and Grijpma D W 2010 Effects of the architecture of tissue engineering scaffolds on cell seeding and culturing *Acta Biomater* **6** 4208–17

[19] Yilgor P, Sousa R A, Reis R L, Hasirci N and Hasirci V 2010 Effect of scaffold architecture and BMP-2/BMP-7 delivery on in vitro bone regeneration *J Mater Sci Mater Med* **21** 2999–3008

[20] Correia C, Bhumiratana S, Yan L P, Oliveira A L, Gimble J M, Rockwood D, Kaplan D L, Sousa R A, Reis R L and Vunjak-Novakovic G 2012 Development of silk-based scaffolds for tissue engineering of bone from human adipose-derived stem cells *Acta Biomater* **8** 2483–92

[21] Ali D 2019 Effect of scaffold architecture on cell seeding efficiency: A discrete phase model CFD analysis *Comput Biol Med* **109** 62–9

[22] Szklanny A A, Debbi L, Merdler U, Neale D, Muñiz A, Kaplan B, Guo S, Lahann J and Levenberg S 2020 High-Throughput Scaffold System for Studying the Effect of Local Geometry and Topology on the Development and Orientation of Sprouting Blood Vessels *Adv Funct Mater* **30** 1901335

[23] Sobral J M, Caridade S G, Sousa R A, Mano J F and Reis R L 2011 Three-dimensional plotted scaffolds with controlled pore size gradients: Effect of scaffold geometry on mechanical performance and cell seeding efficiency *Acta Biomater* **7** 1009–18

[24] Coppola B, Cappetti N, Di Maio L, Scarfato P and Incarnato L 2018 3D Printing of PLA/clay Nanocomposites: Influence of Printing Temperature on Printed Samples Properties *Mater.* **11** 1947

[25] Carlier E, Marquette S, Peerboom C, Denis L, Benali S, Raquez J M, Amighi K and Goole J 2019 Investigation of the parameters used in fused deposition modeling of poly(lactic acid) to optimize 3D printing sessions *Int J Pharm* **565** 367–77

[26] Micó-Vicent B, Perales E, Huraibat K, Martínez-Verdú F M and Viqueira V 2019 Maximization of FDM-3D-Objects Gonio-Appearance Effects Using PLA and ABS Filaments and Combining Several Printing Parameters: "A Case Study" *Mater.* **12** 1423

[27] Anderson J R, Chiu D T, Jackman R J, Cherniavskaya O, McDonald J C, Wu H, Whitesides S H and Whitesides G M 2000 Fabrication of topologically complex three-dimensional microfluidic systems in PDMS by rapid prototyping *Anal Chem* **72** 3158–64

[28] Villegas M, Cetinic Z, Shakeri A and Didar T F 2018 Fabricating smooth PDMS microfluidic channels from low-resolution 3D printed molds using an omniphobic lubricant-infused coating *Anal Chim Acta* **1000** 248–55

[29] Nava M M, Raimondi M T and Pietrabissa R A 2013 A multiphysics 3D model of tissue growth under interstitial perfusion in a tissue-engineering bioreactor *Biomech Model Mechanobiol* **12** 1169–79

[30] Farah S, Anderson D G and Langer R 2016 Physical and mechanical properties of PLA, and their functions in widespread applications - A comprehensive review *Adv Drug Deliv Rev* **107** 367–92

[31] Talò G, Turrisi C, Arrigoni C, Recordati C, Gerges I, Tamplenizza M, Cappelluti A, Riboldi S A and Moretti M 2018 Industrialization of a perfusion bioreactor: Prime example of a non-straightforward process *J Tissue Eng Regen Med* **12** 405–15

[32] Talò G, D'Arrigo D, Lorenzi S, Moretti M and Lovati A B 2020 Independent, Controllable Stretch-Perfusion Bioreactor Chambers to Functionalize Cell-Seeded Decellularized Tendons *Ann Biomed Eng* **48** 1112–26

[33] Cheng M, Moretti M, Engelmayr G C and Freed L E 2009 Insulin-like growth factor-I and slow, bi-directional perfusion enhance the formation of tissue-engineered cardiac grafts *Tissue Eng Part A* **15** 645–53

[34] Mayer N, Lopa S, Talò G, Lovati A B, Pasdeloup M, Riboldi S A, Moretti M and Mallein-Gerin F 2016 Interstitial Perfusion Culture with Specific Soluble Factors Inhibits Type I Collagen Production from Human Osteoarthritic Chondrocytes in Clinical-Grade Collagen Sponges *PLoS One* **11** e0161479

[35] Arrigoni C, Bongio M, Talò G, Bersini S, Enomoto J, Fukuda J and Moretti M 2016 Rational Design of Prevascularized Large 3D Tissue Constructs Using Computational Simulations and Biofabrication of Geometrically Controlled Microvessels *Adv Heal. Mater* **5** 1617–26

[36] Ebeling W, Hennrich N, Klockow M, Metz H, Orth H D and Lang H 1974 Proteinase K from Tritirachium album Limber *Eur J Biochem* **47** 91–7

[37] Tinevez J Y, Perry N, Schindelin J, Hoopes G M, Reynolds G D, Laplantine E, Bednarek S Y, Shorte S L and Eliceiri K W 2017 TrackMate: An open and extensible platform for single-particle tracking *Methods* **115** 80–90

[38] Grémare A, Guduric V, Bareille R, Heroguez V, Latour S, L'heureux N, Fricain J C, Catros S

and Le Nihouannen D 2018 Characterization of printed PLA scaffolds for bone tissue engineering *J Biomed Mater Res A* **106** 887–94

[39] Di Luca A, Ostrowska B, Lorenzo-Moldero I, Lepedda A, Swieszkowski W, Van Blitterswijk C and Moroni L 2016 Gradients in pore size enhance the osteogenic differentiation of human mesenchymal stromal cells in three-dimensional scaffolds *Sci Rep* **6** 22898

[40] Domingos M, Intranuovo F, Russo T, De Santis R, Gloria A, Ambrosio L, Ciurana J and Bartolo P 2013 The first systematic analysis of 3D rapid prototyped poly(ε-caprolactone) scaffolds manufactured through BioCell printing: the effect of pore size and geometry on compressive mechanical behaviour and in vitro hMSC viability *Biofabrication* **5** 045004

[41] Serra T, Planell J A and Navarro M 2013 High-resolution PLA-based composite scaffolds via 3-D printing technology *Acta Biomater* **9** 5521–30

[42] Breuls R G M, Jiya T U and Smit T H 2008 Scaffold Stiffness Influences Cell Behavior: Opportunities for Skeletal Tissue Engineering *Open Orthop. J.*

[43] Arifa K, Rahman M M and Asmatulu E 2018 Mechanical properties of 3D printed PLA specimens with various infill shapes and volumes *TechConnect Briefs 2018 - Advanced Materials*

[44] Lawrenz A, Nason F and Cooper-White J J 2012 Geometrical effects in microfluidic-based microarrays for rapid, efficient single-cell capture of mammalian stem cells and plant cells *Biomicrofluidics* **6** 24112–2411217

[45] Karimi A, Yazdi S and Ardekani A M 2013 Hydrodynamic mechanisms of cell and particle trapping in microfluidics *Biomicrofluidics* **7** 21501

[46] Quent V M C, Loessner D, Friis T, Reichert J C and Hutmacher D W 2010 Discrepancies between metabolic activity and DNA content as tool to assess cell proliferation in cancer research *J. Cell. Mol. Med.*

[47] Chen X, Fan H, Deng X, Wu L, Yi T, Gu L, Zhou C, Fan Y and Zhang X 2018 Scaffold Structural Microenvironmental Cues to Guide Tissue Regeneration in Bone Tissue Applications *Nanomater.* **8** 960

[48] Almeida C R, Serra T, Oliveira M I, Planell J A, Barbosa M A and Navarro M 2014 Impact of 3-D printed PLA- and chitosan-based scaffolds on human monocyte/macrophage responses: unraveling the effect of 3-D structures on inflammation *Acta Biomater* **10** 613–22

[49] Tajsoleiman T, Abdekhodaie M J, Gernaey K V and Krühne U 2018 Efficient Computational Design of a Scaffold for Cartilage Cell Regeneration *Bioeng.* **5** 33

[50] Tang Z, Akiyama Y, Itoga K, Kobayashi J, Yamato M and Okano T 2012 Shear stress-dependent cell detachment from temperature-responsive cell culture surfaces in a microfluidic device *Biomaterials* **33** 7405–11

[51] Stamp M E M, Jötten A M, Kudella P W, Breyer D, Strobl F G, Geislinger T M, Wixforth A and Westerhausen C 2016 Exploring the Limits of Cell Adhesion under Shear Stress within Physiological Conditions and beyond on a Chip *Diagnostics (Basel)* **6** 38

[52] Melchels F P W, Tonnarelli B, Olivares A L, Martin I, Lacroix D, Feijen J, Wendt D J and Grijpma D W 2011 The influence of the scaffold design on the distribution of adhering cells

after perfusion cell seeding *Biomaterials* **32** 2878–84

[53] Raimondi M T, Bertoldi S, Caddeo S, Farè S, Arrigoni C and Moretti M 2016 The effect of polyurethane scaffold surface treatments on the adhesion of chondrocytes subjected to interstitial perfusion culture *Tissue Eng Regen Med* **13** 364–74

[54] Marin A C, Grossi T, Bianchi E, Dubini G and Lacroix D 2017 μ-Particle tracking velocimetry and computational fluid dynamics study of cell seeding within a 3D porous scaffold *J Mech Behav Biomed Mater* **75** 463–9

[55] Wendt D, Marsano A, Jakob M, Heberer M and Martin I 2003 Oscillating perfusion of cell suspensions through three-dimensional scaffolds enhances cell seeding efficiency and uniformity *Biotechnol Bioeng* **84** 205–14

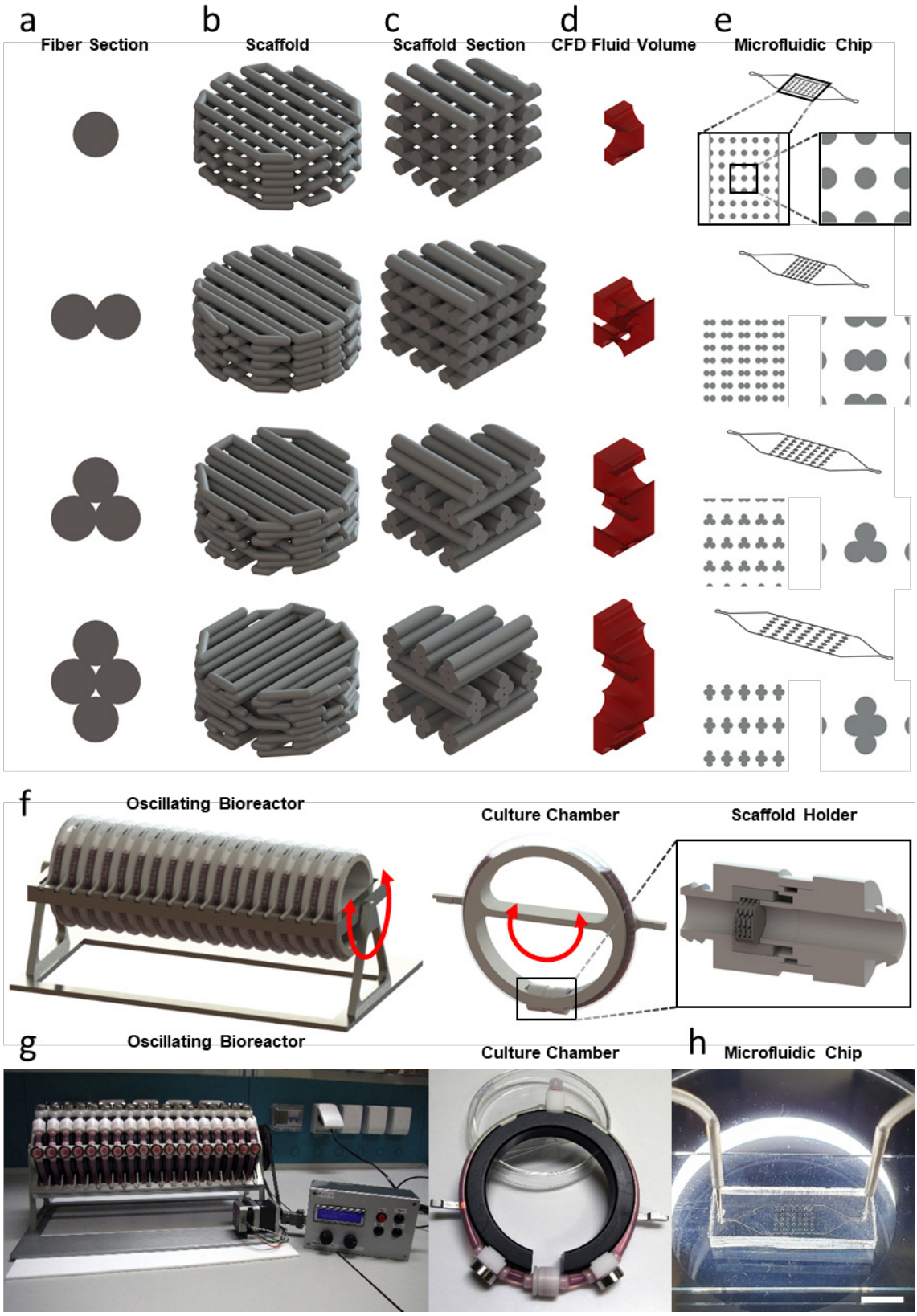

Figure 1 Design overview. CAD sections of circular and multilobed fibers (a) were used to generate the corresponding 3D porous scaffolds (b); sections of scaffolds (c) were used to extract

representative volumes of the fluid for CFD simulations (d); microfluidic chips were designed to model a volumetric section of the structure of the scaffolds (e); dynamic seeding efficiency was evaluated using an oscillating perfusion bioreactor, consisting of a rotating platform to which the culture chambers are connected, that creates a relative movement between the cell suspension and the scaffold contained in the scaffold holder (f, red arrows show the direction of chamber oscillation); real pictures of the oscillating perfusion bioreactor and culture chamber used for cell seeding and culturing experiments (g); real picture of the microfluidic chip with circular pillars used for cell tracking experiments (h, scale bar 2 mm).

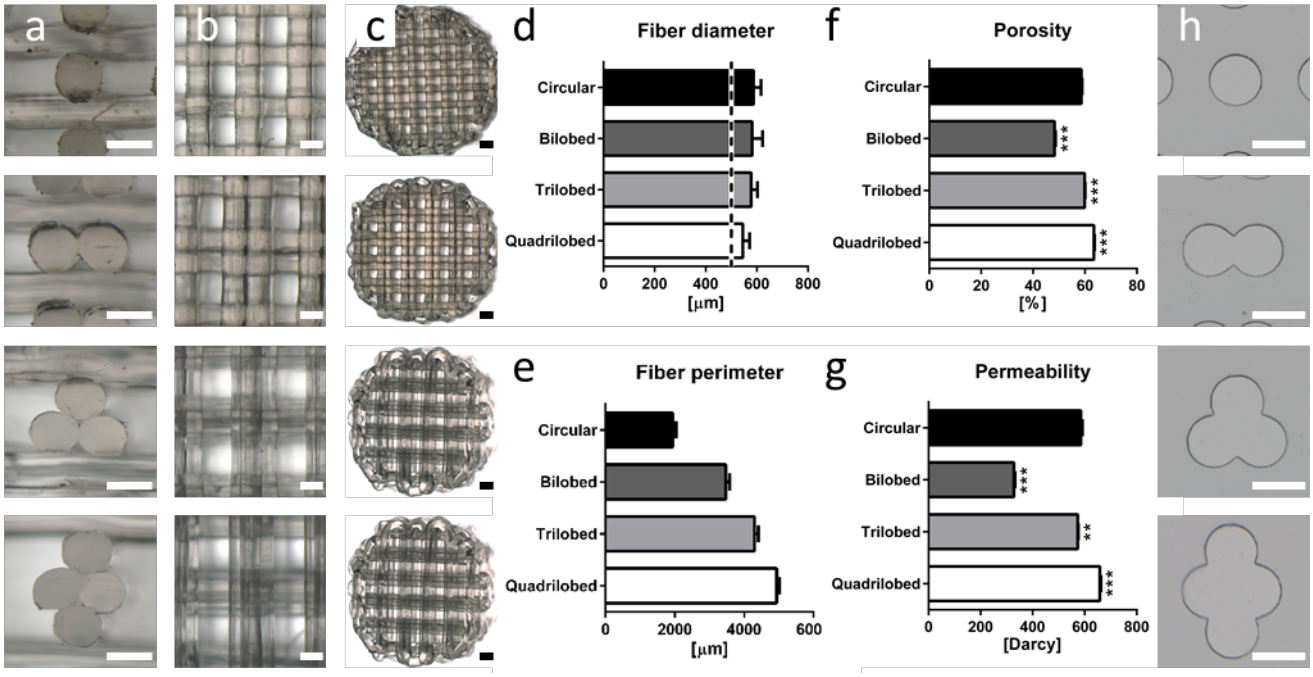

Figure 2 Geometric characterization. Sections of printed fibers (a) and top view of printed scaffolds (b, scale bar 500 µm, c, scale bar 1 mm); evaluation of fiber geometrical parameter: diameter (d) and perimeter (e); evaluation of scaffold geometrical parameter: porosity (f) and permeability (g); top view of microfluidic chip pillars (h, scale bar 500 µm).

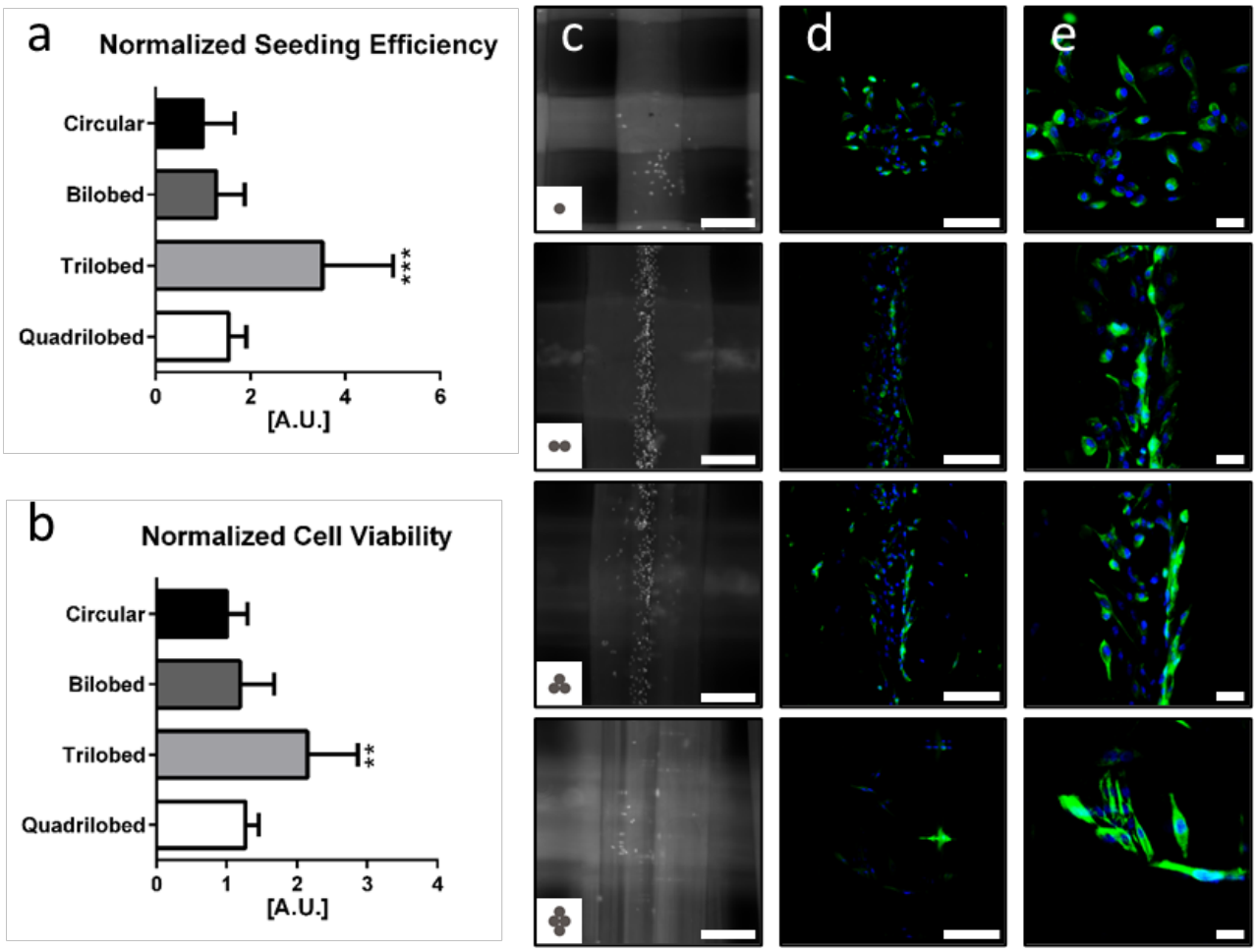

Figure 3 Biological results. Evaluation of normalized seeding efficiency (a) and cell viability (b); top view of cell positioning (c, magnification 4x, scale bar 500 µm).and cell morphology and orientation (d, magnification 10x, scale bar 250 µm; e, magnification 20x, scale bar 25 µm).

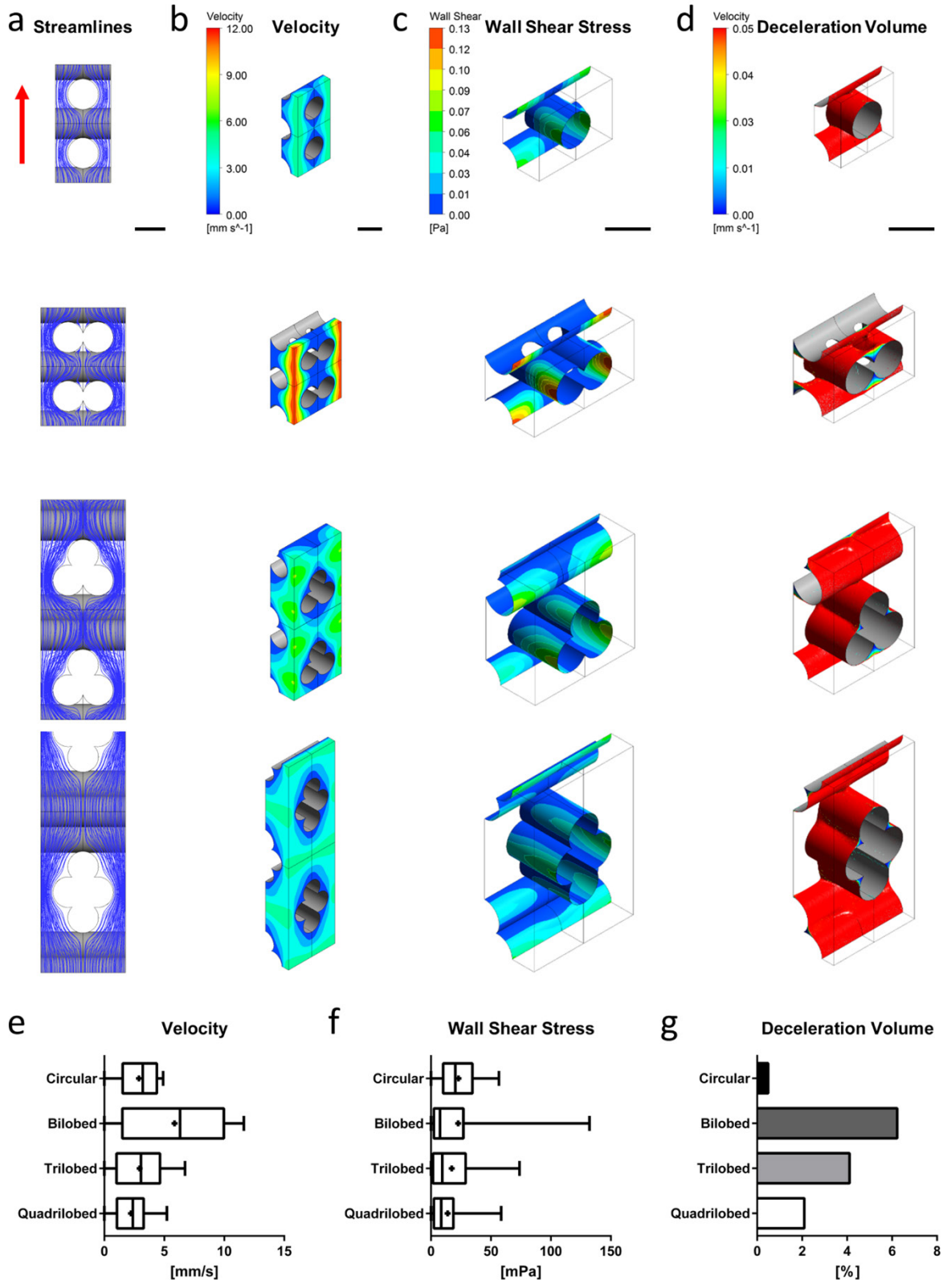
a Streamlines
b Velocity
Velocity
12.00
9.00
6.00
3.00
0.00
[mm s^-1]
c Wall Shear Stress
Wall Shear
0.13
0.12
0.10
0.09
0.07
0.06
0.04
0.03
0.01
0.00
[Pa]
d Deceleration Volume
Velocity
0.05
0.04
0.03
0.01
0.00
[mm s^-1]
e Velocity
Circular
Bilobed
Trilobed
Quadrilobed
0
5
10
15
[mm/s]
f Wall Shear Stress
Circular
Bilobed
Trilobed
Quadrilobed
0
50
100
150
[mPa]
g Deceleration Volume
Circular
Bilobed
Trilobed
Quadrilobed
0
2
4
6
8
[%]

1

Figure 4 Computational results. Fluid dynamic parameters computed through CFD simulations: fluid streamlines (a), shear stress distribution on fiber walls (b), and deceleration volume around the fibers indicating fluid regions characterized by low velocity values (c, scale bar 500 μm, red arrow shows the main flow direction); graphical visualization of analyzed parameters: fluid velocity (d), wall shear stress (e), and deceleration volume (f). Graphs (d) and (e) represent box plots showing min, max and median values; + indicates the mean value; flow in bottom-to-top direction.

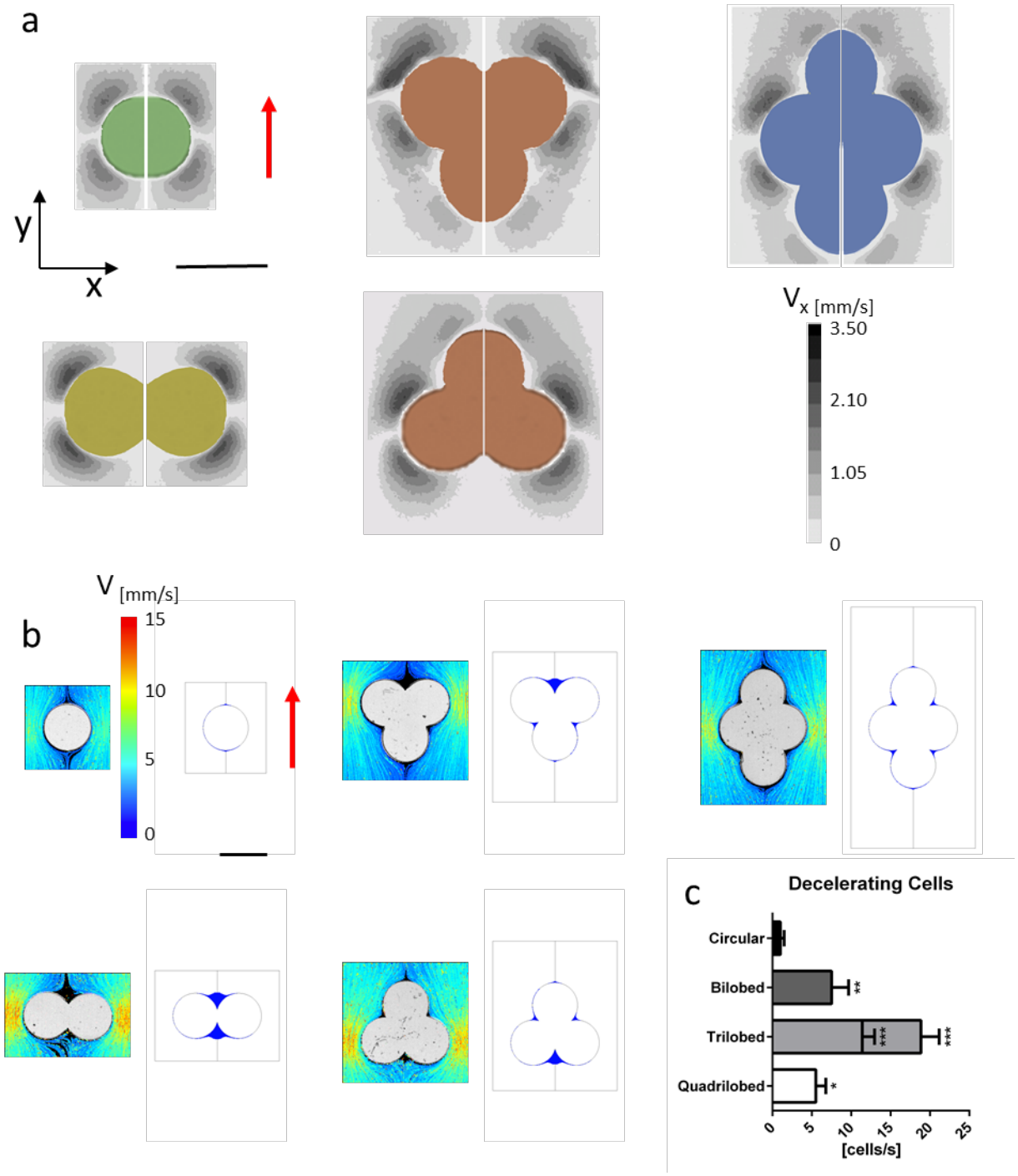

Figure 5 Cell tracking results. Maps of transversal velocity around pillars in microfluidic chip, as results of µPIV analyses (a). Visualization of cell trajectories (color is the local velocity magnitude) around the pillars of microfluidic chips extracted experimentally and relative deceleration areas (blue regions) around the modeled fibers computed through CFD simulations (b, scale bar 500 µm, red

1 arrow shows flow direction); Normalized number of decelerating cells, flowing around the fibers and

2 reaching the deceleration area (c); flow is bottom-to-top direction.

3

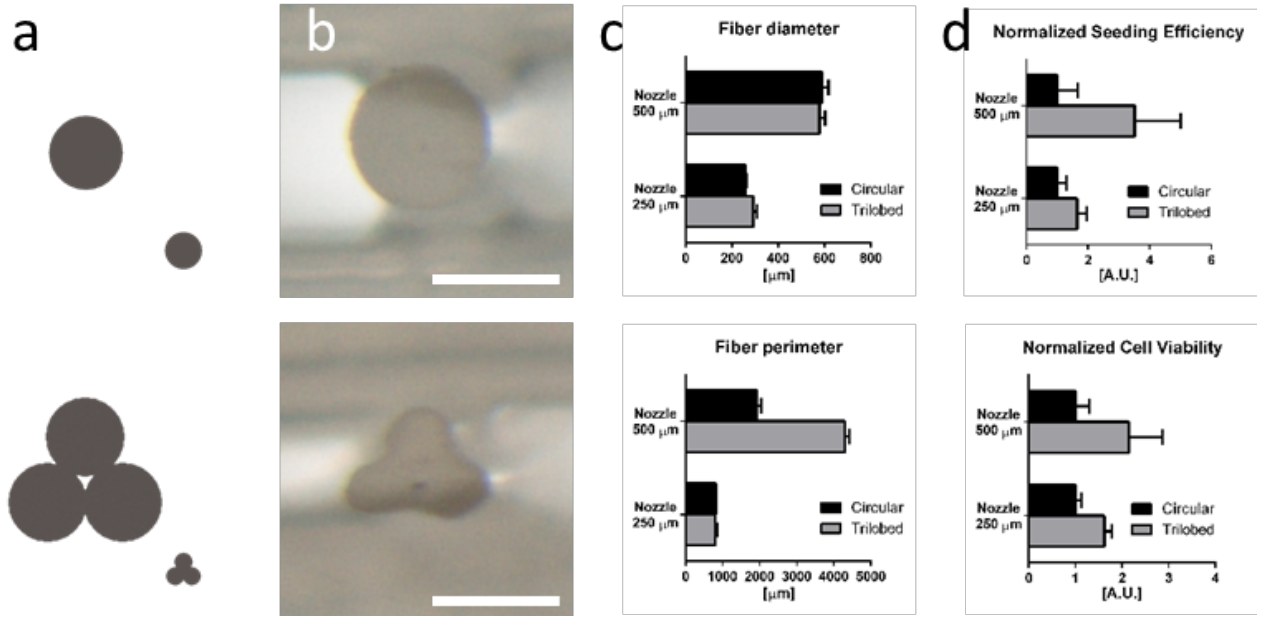

Figure 6 Printing results. Sections of designed fibers (comparison between 500 µm and 250 µm nozzle) (a) and printed fibers(b) obtained with a single deposition step (scale bar 250 µm); comparison of geometrical parameters between assembled fibers (Ø = 500 µm for each cylindrical unit) and extruded fibers (total Ø = 250 µm): fiber diameter and fiber perimeter (c); comparison of normalized seeding efficiency and cell viability (d) between assembled fibers (Ø = 500 µm each) and extruded fibers (Ø = 250 µm).